Case Studies in Thermal Engineering 27 (2021) 101351

Contents lists available at ScienceDirect

Case Studies in Thermal Engineering

journal homepage: www.elsevier.com/locate/csite

Scalings for unsteady natural convection boundary layer under time-varying heating flux in a small Prandtl number fluid

Wenxian Lin [a,*], S.W. Armfield [b], Mehdi Khatamifar [a]

[a] College of Science and Engineering, James Cook University, Townsville, QLD 4811, Australia
[b] School of Aerospace, Mechanical and Mechatronic Engineering, The University of Sydney, NSW 2006, Australia

ARTICLE INFO

Keywords:
Natural convection
Boundary layer
Scaling
Time-varying heat flux
Small Prandtl number

ABSTRACT

The unsteady natural convection boundary layer (NCBL) on a vertical wall heated by time-varying flux in initially quiescent homogeneous fluid with a small Prandtl number (Pr) was studied. Scalings for the parameters typifying NCBL behavior, including plate temperature, maximum vertical velocity, thermal boundary-layer thickness, and velocity boundary-layer thickness, at different development stages, and the time for the transition from the start-up stage to the quasi-steady state, were developed by scaling analysis. The obtained scalings were compared to and validated by the numerical results with different values of Pr, the Rayleigh number Ra and the dimensionless time-varying heat flux frequency f_n, over $10^6 \leq \mathrm{Ra} \leq 10^9$, $0.01 \leq \mathrm{Pr} \leq 0.5$, and $0.001 \leq f_n \leq 0.025$. It is also found that the development of the boundary layer at the start-up stage is one-dimensional and but becomes two-dimensional at the quasi-steady state.

1. Introduction

In numerous practical applications, the unsteady NCBL and heat transfer are caused by a time-varying flux or temperature. One exemplary case is in a passive solar house where the vertical Trombe wall painted in black or with a solar selective coating is heated by time-varying heat flux in the form of solar radiation, which varies sinusoidally under a clear sky condition (only in the first half of the sinusoidal cycle), which produces the NCBL of air transferring the absorbed heat to the space of the house [1]. The understanding of the unsteady NCBL and the associated heat transfer produced by time-varying heating conditions is still limited, although there have been some studies on the topic (*e.g.*, Refs. [2–12]) and a summary of some of these studies can be found in Ref. [3].

Saha, Brown & Gu [7] carried out scaling analysis to give the scalings for unsteady NCBL adjacent to a vertical flat plate for fluids with the Prandtl number (Pr) larger than 1 subject to ramp surface heat flux which increases with time up to some specific time and then remains constant, and validated the obtained scalings with their numerical simulation results. Hattori, Patterson & Lei [13] studied the characterization of linear and oscillatory behaviours of the NCBL induced by the absorption of time-varying solar radiation, and obtained the time and frequency scales of the unstable thermal boundary layer. A series of studies have been conducted recently by Liu and his co-workers [10,14,15] on the unsteady natural convection flow subject to linear thermal forcing. They used scaling analysis to develop various scalings to characterize the unsteady natural convection behavior and verified them with numerical simulation results. Zhou et al. [16] investigated numerically the unsteady NCBL in a cavity with time-varying thermal forcing on a sidewall which varies sinusoidally with time and found that the flow behavior is governed by three characteristic time scales including the forcing

---

* Corresponding author.
E-mail address: wenxian.lin@jcu.edu.au (W. Lin).

https://doi.org/10.1016/j.csite.2021.101351
Received 25 April 2021; Received in revised form 22 July 2021; Accepted 14 August 2021
Available online 17 August 2021

period. Loenko, Shenoy & Sheremet [17] carried out a numerical study on the effect of the wall temperature, which changes with time sinusoidally, on the unsteady natural convection of a non-Newtonian fluid in an enclosure, and found that a pseudoplastic fluid with large Ra values and large oscillation frequencies is more favorable for enhancing the convective heat and mass transfer. We and our co-workers have carried out a series of studies on the unsteady NCBL of either a homogenous or a stratified $\mathrm{Pr} > 1$ or $\mathrm{Pr} < 1$ fluid on a vertical plate subject to different time-varying heat flux or temperature over a wide range of Ra, Pr, thermal forcing frequency, and stratification extent, and obtained various scalings characterizing the NCBL behavior through scaling analysis which were found to agree well with numerical simulation results [2–4,11,18]. For example, we obtained the scalings through scaling analysis for the unsteady NCBL of a homogeneous Newtonian fluid with $\mathrm{Pr} > 1$ on a vertical plate heated with time-varying sinusoidal heat flux and validated them with numerical simulation results [3]. The results show that the transient flow dynamics and heat transfer characteristics of the unsteady NCBL are well predicted and quantified by these scalings in terms of the governing parameters including Ra, Pr, and the frequency of the time-varying heating flux.

There are some studies on the unsteady NCBL on inclined plates, also subject to time-varying heating conditions. Fohr & Moussa [19] studied experimentally and numerically the NCBL and heat transfer in a cylindrical grain silo which was heated with time-dependent solar radiation. Wang, Zeng & Wang [5] studied numerically the three-dimensional unsteady NCBL in an inclined porous cavity heated by time-dependent sinusoidal oscillating temperature and examined the influence of inclination angle and temperature oscillation frequency on the NCBL characteristics at intermediate Rayleigh number (Ra) of 10^6 and 10^7. They also conducted an experimental study on the unsteady NCBL in an inclined enclosure with time-periodically-varying wall temperature [6]. Yu, Patterson & Lei [20] numerically studied the unsteady natural convection in a triangular domain induced by ramped iso-flux cooling at the water surface and presented qualitative and quantitative results showing the effects of the ramp time on the transient behaviour at different Rayleigh numbers. Saha, Patterson & Lei [21] and Mao, Lei & Patterson [22] used scaling analysis and numerical simulations to study the unsteady behavior of NCBL in similar configurations (in attics and reservoir sidearm) subject to time-varying heating conditions.

In our previous study [23], the transient behavior of the NCBL of a homogeneous fluid with $\mathrm{Pr} < 1$ on a vertical wall heated by constant flux was examined by scaling analysis and numerical simulation. This previous work is extended in the present study to the situation when the applied heat flux is time-varying in the sinusoidal form.

2. Scalings

The considered problem is the two-dimensional (2D) unsteady NCBL of a homogeneous $\mathrm{Pr} < 1$ fluid on a vertical wall of height H, heated by a time-varying flux, as sketched in Fig. 1(a). The flux is quantified by the following time-varying temperature gradient across the wall $T_X^0(t)$,

$$T_X^0(t) = \left.\frac{dT}{dX}\right|_{X=0} = -\Gamma_w(t) = -\Gamma_{wm}\sin(2\pi f t), \tag{1}$$

in which T is temperature, X the horizontal coordinate, $\Gamma_w(t)$ the temperature gradient across the wall at time t with the maximum value Γ_{wm}, and f the frequency of the heating flux, respectively. The wall is of no thickness, with its bottom tip at the origin where $X =$

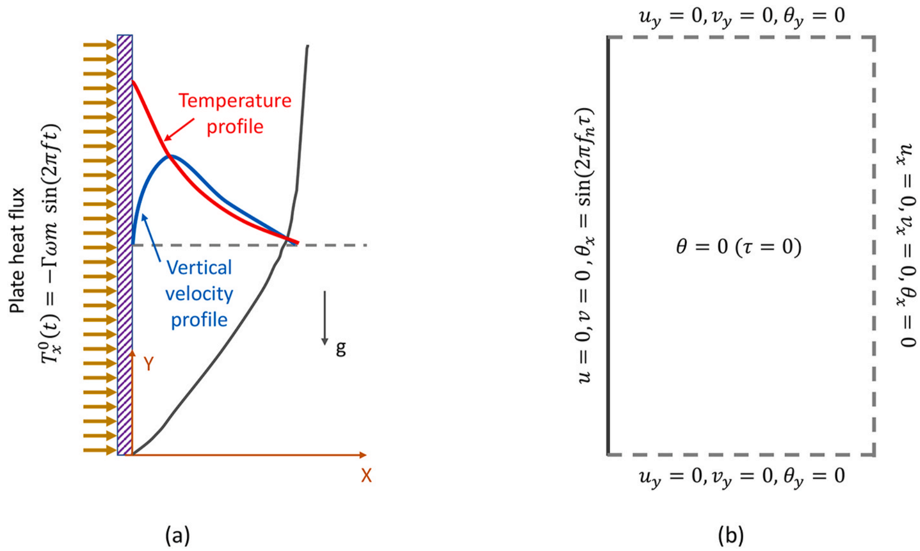

Fig. 1. (a) Sketch of the NCBL flow with the temperature and vertical velocity profiles and (b) the initial and boundary conditions for the computational domain. All parameters in (b) are dimensionless and the subscripts 'x' and 'y' represent the first derivatives with respect to x and y, respectively.

0 and $Y = 0$ (Y is the vertical coordinate). The boundary conditions on the wall are,

$$U = V = 0, \ \frac{dT}{dX} = -\Gamma_{wm}\sin(2\pi f t), \tag{2}$$

where U and V are the velocity components in the X and Y directions.

The equations of the flow and heat transfer are the 2D Navier-Stokes equations with the Boussinesq approximation for buoyancy and the temperature equation. The flow is governed by Pr, Ra, and f_n, which is the dimensionless frequency of the flux, defined as follows,

$$\mathrm{Pr} = \frac{\nu}{\kappa}, \quad \mathrm{Ra} = \frac{g\beta\overline{\Gamma}_w H^4}{\nu\kappa}, \quad f_n = \frac{f}{V_0/H} = \frac{0.5/t_{total}}{V_0/H} = \frac{0.5}{\tau_{total}}, \tag{3}$$

in which g is the acceleration of gravity, β, ν and κ are the thermal expansion coefficient, kinematic viscosity and thermal diffusivity of fluid, and $\overline{\Gamma}_w$ is the time-averaged temperature gradient at the wall, *i.e.*,

$$\overline{\Gamma}_w = \frac{1}{t_{total}}\int_0^{t_{total}} \Gamma_{wm}\sin(2\pi f t)dt = \frac{2}{\pi}\Gamma_{wm}, \tag{4}$$

where t_{total} (s) is the total heating period, which is made dimensionless as $\tau_{total} = t_{total}/(H/V_0)$, and $V_0 = \kappa \mathrm{Ra}^{2/5}/H$ is the characteristic velocity [3,11,24]. Similar to the clear-sky solar radiation model [1], only the first half, heating cycle is considered here, hence $f_n = 0.5/\tau_{total}$.

As shown in the previous studies [3,11,18,23], the unsteady NCBL on a heated vertical wall develops from the initial unsteady start-up stage to the fully developed, quasi-steady state. The transient NCBL behavior is typified by four characteristics parameters, *i.e.*, δ_T (the thermal boundary-layer thickness), θ_w (the wall temperature), v_m (the maximum velocity), and δ_{vi} (the inner velocity boundary-layer thickness, *i.e.*, the distance from the wall to the location v_m occurs). These parameters are made dimensionless by their corresponding characteristic scales, *i.e.*, H, $\Gamma_w H$, V_0, and H, respectively.

Scalings related these parameters to Ra, Pr and f_n can be developed using scaling analysis by evaluating the magnitudes of the terms in the governing equations. In the present study, the scaling analysis follows the same procedure that we used for unsteady NCBL under a range of heating conditions and configurations [3,4,11,23–27], and particularly, that used in Ref. [23], as it is the extension from Ref. [23] which deals with the same NCBL flow problem but the applied heat flux is constant (*i.e.*, T_X^0 is fixed). More specifically, the same scaling analysis procedure detailed in Ref. [23] is followed step-by-step in the presented study by replacing the constant T_X^0 used in Ref. [23] with the time-varying $T_X^0(t)$ given by Eq. (1). To avoid repetition, only the outcomes from this scaling analysis are presented here. The details of the scaling analysis procedure can be found in Ref. [23].

The scaling analysis for the present study yields the following scalings for the four characteristics parameters at different development stages.

At the start-up stage when the flow is unsteady,

$$\delta_T \sim \frac{\tau^{1/2}}{\mathrm{Ra}^{1/5}}, \tag{5}$$

$$\theta_w \sim \frac{\sin(2\pi f_n \tau)\tau^{1/2}}{\mathrm{Ra}^{1/5}}, \tag{6}$$

$$\delta_{vi} \sim \frac{\mathrm{Pr}^{1/2}\tau^{1/2}}{\mathrm{Ra}^{1/5}} \tag{7}$$

$$v_m \sim \frac{\sin(2\pi f_n \tau)\mathrm{Pr}\ \tau^{3/2}}{[O(1) + O(\mathrm{Pr})]}. \tag{8}$$

The time for transition to the quasi-steady state is

$$\tau_s \sim \frac{[O(1) + O(\mathrm{Pr})]^{2/5} y^{2/5}}{[\sin(2\pi f_n \tau)]^{2/5}\mathrm{Pr}^{2/5}}, \tag{9}$$

and at the quasi-steady state when the flow becomes fully developed, steady,

$$\delta_{T,s} \sim \frac{[O(1) + O(\mathrm{Pr})]^{1/5} y^{1/5}}{[\sin(2\pi f_n \tau_s)]^{1/5}\mathrm{Ra}^{1/5}\mathrm{Pr}^{1/5}}, \tag{10}$$

$$\theta_{w,s} \sim \frac{[\sin(2\pi f_n \tau_s)]^{4/5}[O(1) + O(\mathrm{Pr})]^{1/5} y^{1/5}}{\mathrm{Ra}^{1/5}\mathrm{Pr}^{1/5}}, \tag{11}$$

$$\delta_{vi,s} \sim \frac{[O(1)+O(\mathrm{Pr}\,)]^{1/5}\mathrm{Pr}^{\,1/2}y^{1/5}}{[\sin(2\pi f_n\tau_s)]^{1/5}\mathrm{Ra}^{1/5}\mathrm{Pr}^{\,1/5}}, \tag{12}$$

$$v_{m,s} \sim \frac{[\sin(2\pi f_n\tau_s)]^{2/5}\mathrm{Pr}^{\,2/5}y^{3/5}}{[O(1)+O(\mathrm{Pr}\,)]^{2/5}}. \tag{13}$$

The function $[O(1) + O(\mathrm{Pr}\,)]$ presented in these scalings represents the contribution from the friction to the inertia when it balances the buoyancy within the boundary layer when *Pr* is smaller than 1, as discussed in Ref. [23].

The obtained scalings show that at the start-up stage the NCBL is one-dimensional (1D) as they do not depend on y. However, they change to 2D as they depend on y at the quasi-steady state.

When the scalings obtained for the present case are compared to those obtained for the case with constant heating flux [23], it is found that only the scalings for δ_T and δ_{vi} at the start-up stage are exactly the same for both cases, and all others differ with the functions of the time-dependent factor $\sin(2\pi f_n\tau)$.

The scalings obtained in the present study for the $\mathrm{Pr} < 1$ case are significantly different from those for the $\mathrm{Pr} > 1$ case as obtained by Lin and Armfield [3]. The comparison of these scalings for both cases is presented in Table 1. It is seen from the table that the dependences of the scalings on Ra, τ, and f_n are the same for both cases, however, their dependences on Pr are significantly different. The dependence on Pr for the $\mathrm{Pr} > 1$ case is in the term of $(1 + \mathrm{Pr}^{-1/2})$, whereas for the $\mathrm{Pr} < 1$ case it is in the term of $[O(1) + O(\mathrm{Pr}\,)]$, due to the different boundary layer structures for both cases. Our previous studies (*e.g.*, [4, 25, 26, 28]) shown that for the $\mathrm{Pr} > 1$ case, the viscous boundary layer is significantly thicker than the thermal boundary layer and a distinct three-region boundary layer structure is present, whereas for the $\mathrm{Pr} < 1$ case, the viscous boundary layer is essentially as thick as the thermal boundary layer and such a three-region boundary layer structure is not applicable.

3. Numerical results and discussion

The above scalings are compared with the numerical simulation results in this section (see Table 1). To validate their individual dependence on Ra, Pr, and f_n, 14 numerical simulation runs were carried out, with the details of these runs presented in Table 2. Runs 1–4 are at four Ra values (10^6, 10^7, 10^8 and 10^9) with $\mathrm{Pr} = 0.1$ and $f_n = 0.01$ to examine the Ra dependence; Runs 3 and 5–10 are at six Pr values (0.01, 0.025, 0.05, 0.075, 0.2 and 0.5) with $\mathrm{Ra} = 10^8$ and $f_n = 0.01$ to demonstrate the Pr dependence; and Runs 3 and 11–14 are at four f_n values (0.001, 0.0025, 0.005 and 0.025) with $\mathrm{Ra} = 10^8$ and $\mathrm{Pr} = 0.1$ to check the f_n dependence. The maximum value of f_n studied is 0.025, as it is found that the required information is not available beyond it. As the scalings are obtained assuming $\mathrm{Pr} \ll 1$ for the validity of the boundary-layer assumption, which was made in the scaling analysis, the Pr values studied are no more than 0.5.

The numerical simulations were performed using the same in-house code used in Ref. [3] and some of our previous studies on NCBL (such as [4,11,18,24–28]). Particularly the computational domain (sketched in Fig. 1(b)) and the mesh used in Ref. [3] (597 × 597 grids) were also used in the present study. As the numerical methods, governing equations, initial and boundary conditions (sketched in Fig. 1(b)), construction of meshes, and benchmarking of the code against the known theoretical results were well documented in those papers, they are not presented here.

3.1. *Quantification of the scalings at the end of the start-up stage*

Fig. 2 presents the typical time series of δ_T, θ_w, δ_{vi} and v_m at $y = 0.5$ for Run 3. It is seen that δ_T, θ_w, and v_m end their respective start-up stage at almost the same time, τ_s, which is determined as the instant when δ_T attains the maximum for the first time, after the start-

Table 1
A comparison of the scaling laws between the current case for $\mathrm{Pr} < 1$ and the case for $\mathrm{Pr} > 1$ [3].

Parameter	The current case for $\mathrm{Pr} < 1$	The case for $\mathrm{Pr} > 1$ [3]
δ_T	$\sim \frac{\tau^{1/2}}{\mathrm{Ra}^{1/5}}$	$\sim \frac{\tau^{1/2}}{\mathrm{Ra}^{1/5}}$
θ_w	$\sim \frac{\sin(2\pi f_n\tau)\tau^{1/2}}{\mathrm{Ra}^{1/5}}$	$\sim \frac{\sin(2\pi f_n\tau)\tau^{1/2}}{\mathrm{Ra}^{1/5}}$
δ_{vi}	$\sim \frac{\mathrm{Pr}^{\,1/2}\tau^{1/2}}{\mathrm{Ra}^{1/5}}$	$\sim \frac{\tau^{1/2}}{(1+\mathrm{Pr}^{\,-1/2})\mathrm{Ra}^{1/5}}$
v_m	$\sim \frac{\sin(2\pi f_n\tau)\mathrm{Pr}\,\tau^{3/2}}{[O(1)+O(\mathrm{Pr}\,)]}$	$\sim \frac{\sin(2\pi f_n\tau)\tau^{3/2}}{(1+\mathrm{Pr}^{\,-1/2})^2}$
τ_s	$\sim \frac{[O(1)+O(\mathrm{Pr}\,)]^{2/5}y^{2/5}}{[\sin(2\pi f_n\tau_s)]^{2/5}\mathrm{Pr}^{\,2/5}}$	$\sim \frac{(1+\mathrm{Pr}^{\,-1/2})^{4/5}y^{2/5}}{[\sin(2\pi f_n\tau_s)]^{2/5}}$
$\delta_{T,s}$	$\sim \frac{[O(1)+O(\mathrm{Pr}\,)]^{1/5}y^{1/5}}{[\sin(2\pi f_n\tau_s)]^{1/5}\mathrm{Ra}^{1/5}\mathrm{Pr}^{\,1/5}}$	$\sim \frac{(1+\mathrm{Pr}^{\,-1/2})^{2/5}y^{1/5}}{[\sin(2\pi f_n\tau_s)]^{1/5}\mathrm{Ra}^{1/5}}$
$\theta_{w,s}$	$\sim \frac{[\sin(2\pi f_n\tau_s)]^{4/5}[O(1)+O(\mathrm{Pr}\,)]^{1/5}y^{1/5}}{\mathrm{Ra}^{1/5}\mathrm{Pr}^{\,1/5}}$	$\sim \frac{[\sin(2\pi f_n\tau_s)]^{4/5}(1+\mathrm{Pr}^{\,-1/2})^{2/5}y^{1/5}}{\mathrm{Ra}^{1/5}}$
$\delta_{vi,s}$	$\sim \frac{\mathrm{Pr}^{\,1/2}[O(1)+O(\mathrm{Pr}\,)]^{1/5}y^{1/5}}{[\sin(2\pi f_n\tau)]^{1/5}\mathrm{Ra}^{1/5}\mathrm{Pr}^{\,1/5}}$	$\sim \frac{y^{1/5}}{(1+\mathrm{Pr}^{\,-1/2})^{3/5}[\sin(2\pi f_n\tau_s)]^{1/5}\mathrm{Ra}^{1/5}}$
$v_{m,s}$	$\sim \frac{[\sin(2\pi f_n\tau_s)]^{2/5}\mathrm{Pr}^{\,2/5}y^{3/5}}{[O(1)+O(\mathrm{Pr}\,)]^{2/5}}$	$\sim \frac{[\sin(2\pi f_n\tau)]^{2/5}y^{3/5}}{(1+\mathrm{Pr}^{\,-1/2})^{4/5}}$

Table 2
Values of Ra, Pr, f_n and τ_{total} for the 14 numerical simulation runs.

Run	Ra	Pr	f_n	τ_{total}
1	10^6	0.1	0.01	50
2	10^7	0.1	0.01	50
3	10^8	0.1	0.01	50
4	10^9	0.1	0.01	50
5	10^8	0.01	0.01	50
6	10^8	0.025	0.01	50
7	10^8	0.05	0.01	50
8	10^8	0.075	0.01	50
9	10^8	0.2	0.01	50
10	10^8	0.5	0.01	50
11	10^8	0.1	0.001	500
12	10^8	0.1	0.0025	200
13	10^8	0.1	0.005	100
14	10^8	0.1	0.025	20

up stage. However, δ_{vi} attains its maximum for the first time, after the start-up stage, at an earlier instant, τ_{vi}. This is because the inner viscous boundary layer is closer to the wall and accordingly undergoes the development earlier. It is therefore appropriate to use τ_s as the time scale for the end of the start-up stage for δ_T, θ_w, and v_m while to use τ_{vi} for δ_{vi}, in the subsequent analysis of the results.

Fig. 3 presents the numerically obtained results for τ_s, $\delta_{T,s}$, $\theta_{w,s}$, and $v_{m,s}$, plotted against the values calculated with their respective scalings at the end of the start-up stage with the numerical results, *i.e.*, from (5), (10), (11), and (13),

$$\widehat{\tau}_s = \frac{y^{2/5}}{[\sin(2\pi f_n \tau_s)]^{2/5}\mathrm{Pr}^{\ 2/5}}, \tag{14}$$

$$\widehat{\delta}_{T,s} = \frac{y^{1/5}}{[\sin(2\pi f_n \tau_s)]^{1/5}\mathrm{Ra}^{1/5}\mathrm{Pr}^{\ 1/5}}, \tag{15}$$

$$\widehat{\theta}_{w,s} = \frac{[\sin(2\pi f_n \tau_s)]^{4/5} y^{1/5}}{\mathrm{Ra}^{1/5}\mathrm{Pr}^{\ 1/5}}, \tag{16}$$

$$\widehat{v}_{m,s} = [\sin(2\pi f_n \tau_s)\,]^{2/5} Pr^{\ 2/5} y^{3/5}. \tag{17}$$

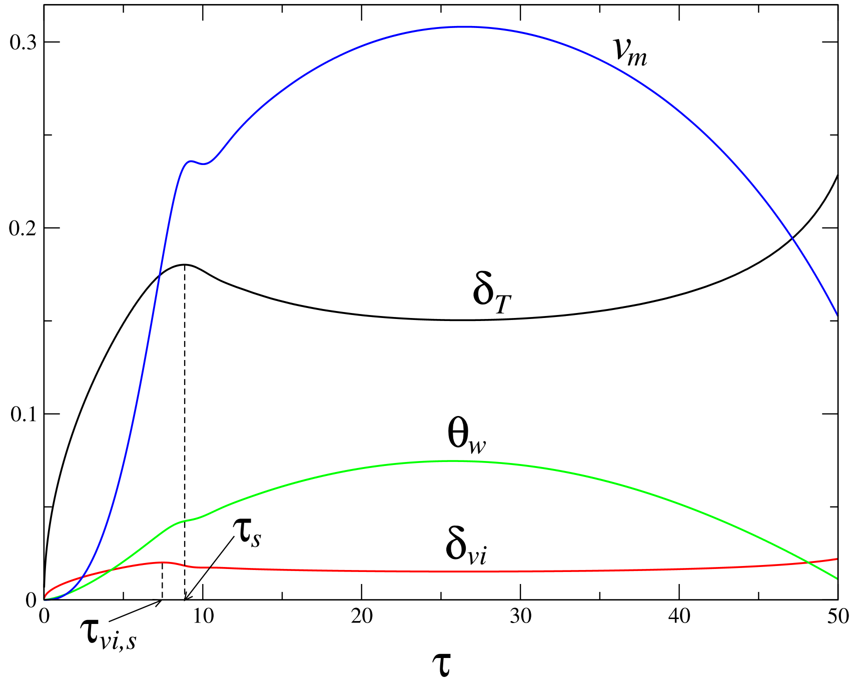

Fig. 2. Typical time series of δ_T, θ_w, δ_{vi} and v_m at $y = 0.5$ for Run 3.

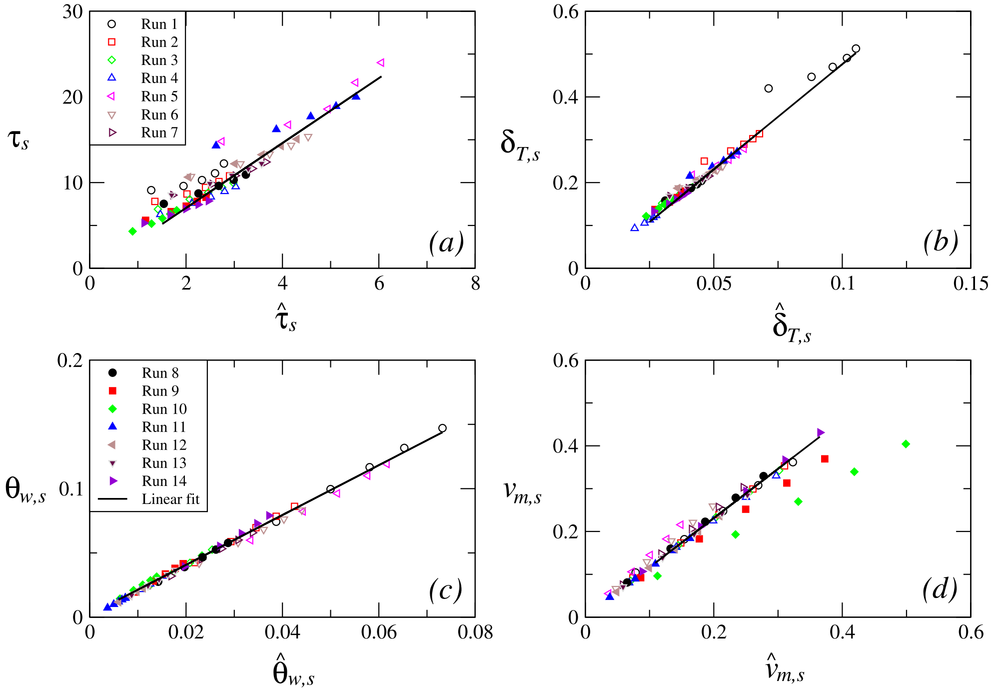

Fig. 3. (*a*) τ_s plotted against $\widehat{\tau}_s$, (*b*) $\delta_{T,s}$ plotted against $\widehat{\delta}_{T,s}$, (*c*) $\theta_{w,s}$ plotted against $\widehat{\theta}_{w,s}$, (*d*) $v_{m,s}$ plotted against $\widehat{v}_{m,s}$. The linear fits in (*a*)-(*c*) are obtained with linear regression by excluding the data at $y = 0.1$ and $y = 0.3$ for all runs and that in (*d*) by excluding Runs 5, 6, 9, 10 and all data at $y = 0.1$ and $y = 0.3$ for the remaining runs.

In the above equations, all $[O(1) + O(\text{Pr})]$ terms are omitted as their effects will be accounted for in the subsequent quantification of each scaling involved. From the figure, it is seen that, after the exclusions of the numerical results at small y values ($y = 0.1$ and 0.3) for all runs and for $v_{m,s}$ with an additional strong Pr effect (the reason for such exclusions will be discussed in the subsequent sections), the scalings (5), (10), (11), and (13), collapse their corresponding quantified relations of τ_s against $\widehat{\tau}_s$, $\delta_{T,s}$ against $\widehat{\delta}_{T,s}$, $\theta_{w,s}$ against $\widehat{\theta}_{w,s}$, $v_{m,s}$ against $\widehat{v}_{m,s}$ with the numerical results, onto a straight line, *i.e.*,

$$\tau_s = 3.785\widehat{\tau}_s - 0.524, \tag{18}$$

$$\delta_{T,s} = 4.909\widehat{\delta}_{T,s} - 0.0146, \tag{19}$$

$$\theta_{w,s} = 1.937\widehat{\theta}_{w,s} + 0.00198, \tag{20}$$

$$v_{m,s} = 1.149\widehat{v}_{m,s} + 0.0016, \tag{21}$$

with the coefficients of regression of 0.9789, 0.9978, 0.9977, and 0.9935, respectively. These results clearly show that (5), (10), (11), and (13) are the correct scalings for τ_s, and $\delta_{T,s}$, $\theta_{w,s}$, and $v_{m,s}$ at τ_s, respectively.

Similarly, the numerical results also validate the scalings (9) and (12). This is demonstrated by the numerical results presented in Fig. 4, which, after the exclusion of the data at small y values ($y = 0.1$ and 0.3) and with additional strong Pr effects, shows that

$$\tau_{vi,s} = 2.972\widehat{\tau}_{vi,s} - 0.3707, \tag{22}$$

$$\delta_{vi,s} = 1.495\widehat{\delta}_{vi,s} + 0.00116, \tag{23}$$

with the coefficients of regression of 0.9984 and 0.9995, respectively. In the above equations, $\widehat{\tau}_{vi,s}$ and $\widehat{\delta}_{vi,s}$ are as follows,

$$\widehat{\tau}_{vi,s} = \frac{y^{2/5}}{\left[\sin\left(2\pi f_n \tau_{vi,s}\right)\right]^{2/5}\text{Pr}^{\,2/5}}, \tag{24}$$

$$\widehat{\delta}_{vi,s} = \frac{\text{Pr}^{\,1/2} y^{1/5}}{\left[\sin\left(2\pi f_n \tau_{vi,s}\right)\right]^{1/5}\text{Ra}^{1/5}\text{Pr}^{\,1/5}}. \tag{25}$$

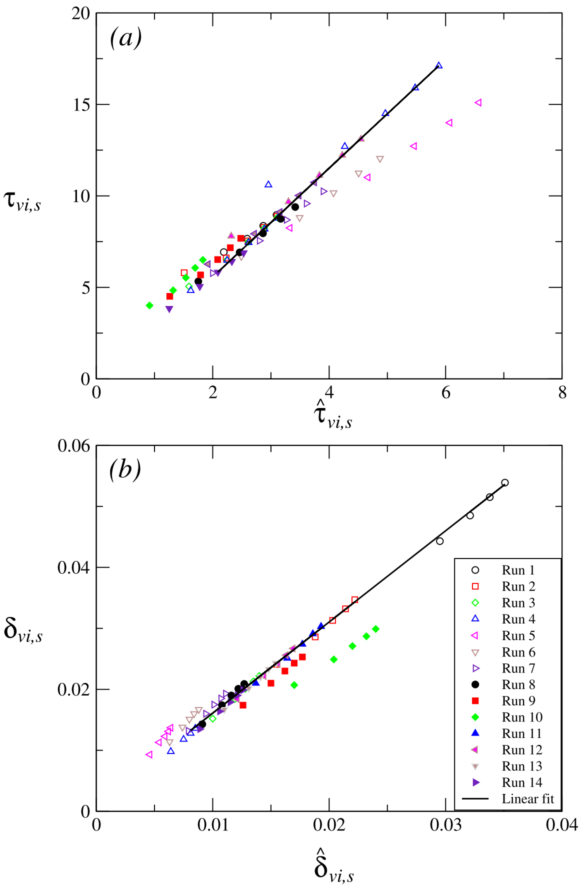

Fig. 4. (*a*) $\tau_{vi,s}$ plotted against $\widehat{\tau}_{vi,s}$ and (*b*) $\delta_{vi,s}$ plotted against $\widehat{\delta}_{vi,s}$. The linear fits are obtained with linear regression by excluding Runs 5, 6, 7, 9, 10 and all data at $y = 0.1$ and $y = 0.3$ for the remaining runs.

3.2. Scalings for δ_T

Fig. 5 illustrates the time series of δ_T with varying y. δ_T is determined as the distance between the wall and the x location where the local temperature reduces to 1% of the wall temperature. At the start-up stage, the scaling (5) for δ_T predicts that the time series of δ_T depends on Ra only. The numerical results shown in Fig. 5(*a*) verify this, as the time series of all runs with the same Ra value ($Ra = 10^8$) are the same before the end of their individual start-up stage, while the times series with $Ra = 10^6$, $Ra = 10^7$ and $Ra = 10^9$ are substantially different from those with $Ra = 10^8$. The 1D behavior of the NCBL at the start-up stage is also clearly demonstrated as the time series with the same Ra value ($Ra = 10^8$), which are at different heights, are the same before the end of their individual start-up stage, indicating they are not y dependent. At the quasi-steady stage, all time series are different, showing the 2D behavior as they become y dependent, as predicted correctly by the scaling (10).

From Eq. (5), it is apparent that $\delta_{T,s} \sim \tau_s^{1/2}/Ra^{1/5}$, hence,

$$\frac{\delta_T}{\delta_{T,s}} \sim \frac{\tau^{1/2}/Ra^{1/5}}{\tau_s^{1/2}\Big/Ra^{1/5}} \sim \frac{\tau^{1/2}}{\tau_s^{1/2}}, \tag{26}$$

which also means that

$$\frac{\delta_T}{\widehat{\delta}_{T,s}} \sim \frac{\tau^{1/2}}{\widehat{\tau}_s^{1/2}}. \tag{27}$$

This is affirmed by the numerical simulation results shown in Fig. 5(*b*), which demonstrates that the scaling (27) brings all scaled time series together until $\tau = 0.5\tau_{total}$ (*i.e.*, when the heat flux on the wall attains its maximum value).

At the start-up stage, as presented in Fig. 5(*b*), all scaled time series overlap each other approximately on the single straight line quantified by

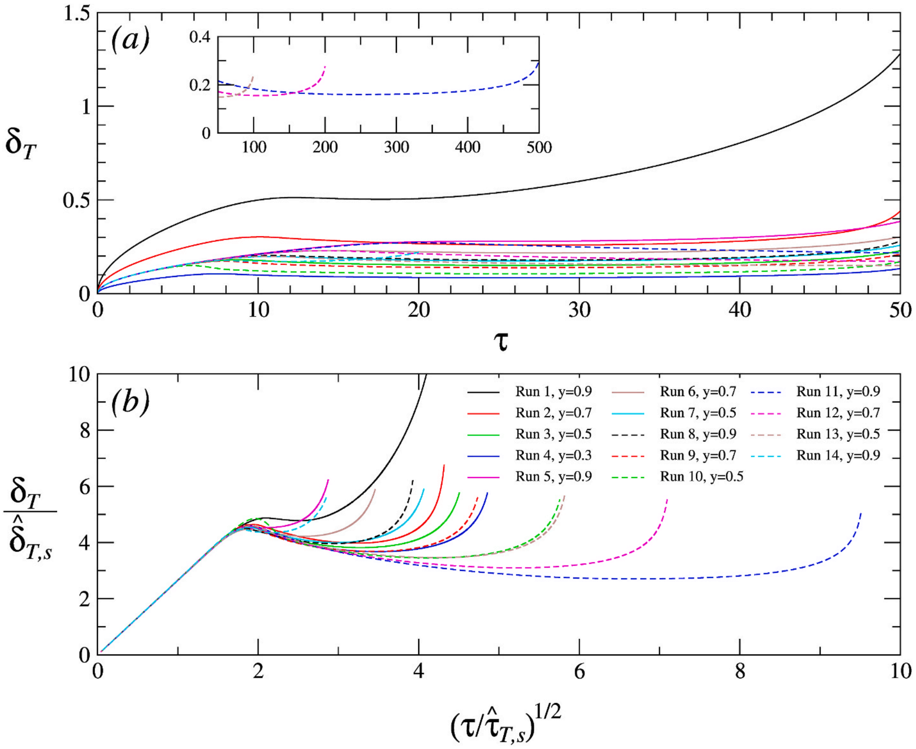

Fig. 5. Time series of δ_T of all numerical simulation runs: (*a*) raw data and (*b*) scaled data with δ_T scaled by $\widehat{\delta}_{T,s} = (y/[(\mathrm{RaPr})\sin(2\pi f_n\tau_s)])^{1/5}$ and τ scaled by $\widehat{\tau}_s = (y/[\mathrm{Pr}\sin(2\pi f_n\tau_s)])^{2/5}$, which are the scalings (10) and (9) for $\delta_{T,s}$ and τ_s, respectively.

$$\frac{\delta_T}{\widehat{\delta}_{T,s}} = 2.646\frac{\tau^{1/2}}{\widehat{\tau}_s^{1/2}}, \tag{28}$$

or, alternatively,

$$\begin{aligned}\delta_T &= 2.646\widehat{\delta}_{T,s}\frac{\tau^{1/2}}{\widehat{\tau}_s^{1/2}}\\ &= 2.646(y/[\mathrm{RaPr}\sin(2\pi f_n\tau_s)])^{1/5}\frac{\tau^{1/2}}{\left[(y/[\mathrm{Pr}\sin(2\pi f_n\tau_s)])^{2/5}\right]^{1/2}}\\ &= 2.646\frac{\tau^{1/2}}{\mathrm{Ra}^{1/5}},\end{aligned} \tag{29}$$

in which 2.646 is the average value of the coefficients of all runs. It is found that the changes of the coefficients from 2.646 among all runs are between -0.4% and 2%, clearly verifying the scaling for δ_T, *i.e.*, Eq. (5). The largest variation (2%) is from the time series with $f_n = 0.025$ (Run 14), which is due to the short total heating period ($\tau_{total} = 20$), leading to a very short quasi-steady state.

At the quasi-steady state, all of the time series overlap well until $\tau = 0.5\tau_{total}$ (*i.e.*, the half of the heating period), which verifies the scalings (10) and (9). It is observed that at the end of the start-up stage, if the results at $y = 0.1$ and 0.3 for all runs and that of Run 1 are excluded, the average value of $\delta_{T,s}/\widehat{\delta}_{T,s}$ is 4.573, with the variations between -2.5% and 6.0%. These results show that the effect of $[O(1) + O(\mathrm{Pr})]$ in the scaling (10) for $\delta_{T,s}$ is minimal. This is the same as that in the case when the applied heat flux is constant [23]. Similarly, the numerical results presented in Fig. 5(*b*) also confirm the scaling (9) for τ_s, which is determined as the time for the time series of δ_T to attain the end of the start-up stage. It is found that $(\tau_s/\widehat{\tau}_s)^{1/2}$ is around 1.887, *i.e.*,

$$\tau_s \approx 3.56\left(\frac{y}{\mathrm{Pr}\,\sin(2\pi f_n\tau_s)}\right)^{2/5}, \tag{30}$$

with the coefficient in the above equation varying within ± 11.5%, if the results at $y = 0.1$ and 0.3 for all runs and that of Run 1 are excluded, indicating the effect of $[O(1) + O(\mathrm{Pr})]$ in the scaling (9) for τ_s, in the case of δ_T, is also not significant. This is again the same as that in the case when the applied heat flux is constant [23].

In Run 1 (with $Ra = 10^6$), δ_T is not much less than y (except at the very early stage), as shown in Fig. 5(a), which means that the boundary-layer assumption is not valid. In fact, if we arbitrarily take the maximum value of $\delta_T \le 0.5y$ as the criterion for the validity of the boundary-layer assumption at height y, it is also observed that all runs at $y = 0.1$, the majority of runs at $y = 0.3$, and a few runs at $y = 0.5$ do not meet the boundary-layer assumption. In the above and the subsequent analysis of the numerical simulation results, those at $y = 0.1$ and 0.3 are thus excluded.

The scalings for θ_w, v_m, and δ_{vi} can be validated in the same way, as described below.

3.3. Scalings for θ_w

At the start-up stage, the scaling (6) shows that Ra and f_n affect θ_w, however, θ_w is independent of Pr and y. The numerical results shown in Fig. 6(a) verify this, with all of the six time series at $Ra = 10^8$ and $f_n = 0.01$, with varying Pr and y (Runs 5–10), overlaying each other at the start-up stage, while there are significant variations in the time series of the runs with different Ra and f_n values. This further illustrates the 1D behavior of the boundary layer at the start-up stage. At the quasi-steady stage, all of the time series are different, agreeing with Eq. (11), which predicts that $\theta_{w,s}$ depends on all these four parameters, and the flow becomes 2D. Similar to δ_T, from the scaling (6), the following relation is expected,

$$\frac{\theta_w}{\theta_{w,s}} \sim \frac{\sin(2\pi f_n \tau)\tau^{1/2} \big/ Ra^{1/5}}{\sin(2\pi f_n \tau_s)\tau_s^{1/2} \big/ Ra^{1/5}} \sim \frac{\sin(2\pi f_n \tau)\tau^{1/2}}{\sin(2\pi f_n \tau_s)\tau_s^{1/2}}, \tag{31}$$

which also indicates that

$$\frac{\theta_w}{\widehat{\theta}_{w,s}} \sim \frac{\sin(2\pi f_n \tau)\tau^{1/2}}{\sin(2\pi f_n \tau_s)\widehat{\tau}_s^{1/2}}. \tag{32}$$

At the start-up stage, as presented in Fig. 6(b), all scaled time series come together on the following single straight line,

$$\frac{\theta_w}{\widehat{\theta}_{w,s}} = 1.191\frac{\sin(2\pi f_n \tau)\tau^{1/2}}{\sin(2\pi f_n \tau_s)\widehat{\tau}_s^{1/2}}, \tag{33}$$

that is,

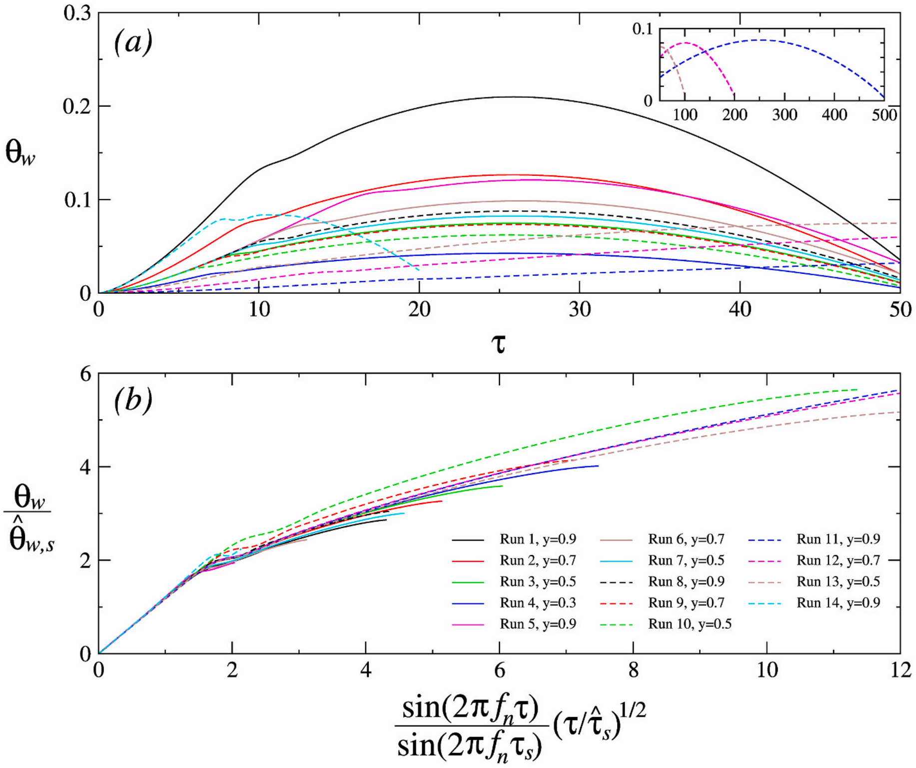

Fig. 6. Time series of θ_w of all numerical simulation runs: (a) raw data and (b) $\theta_w/\widehat{\theta}_{w,s}$ plotted against $[\sin(2\pi f_n\tau)/\sin(2\pi f_n\tau_s)](\tau/\widehat{\tau}_s)^{1/2}$, with θ_w scaled by $\widehat{\theta}_{w,s} = [\sin(2\pi f_n\tau_s)]^{4/5}y^{1/5}/(\mathrm{Ra}^{1/5}\mathrm{Pr}^{\ 1/5})$ and τ scaled by $\widehat{\tau}_s = (y/[\mathrm{Pr}\sin(2\pi f_n\tau_s)])^{2/5}$, which are the scalings (11) and (9) for $\theta_{w,s}$ and τ_s, respectively.

$$\begin{aligned}\theta_w &= 1.191\widehat{\theta}_{w,s}\frac{\sin(2\pi f_n\tau)\tau^{1/2}}{\sin(2\pi f_n\tau_s)\widehat{\tau}_s^{1/2}}\\ &= 1.191\frac{\sin(2\pi f_n\tau_s)\widehat{\tau}_s^{1/2}}{\mathrm{Ra}^{1/5}}\,\frac{\sin(2\pi f_n\tau)\tau^{1/2}}{\sin(2\pi f_n\tau_s)\widehat{\tau}_s^{1/2}}\\ &= 1.191\frac{\sin(2\pi f_n\tau)\tau^{1/2}}{\mathrm{Ra}^{1/5}},\end{aligned} \tag{34}$$

in which 1.191 is the average value of the coefficients of all runs. The changes of the coefficients from 1.191 among all runs are between -1.7% and 3.2%, clearly verifying the scaling for θ_w, *i.e.*, Eq. (6). The largest variation (3.2%) is again from the time series with $f_n = 0.025$ (Run 14), due to the same reason as mentioned above.

At the quasi-steady stage, the majority of the scaled time series of $\theta_w/\widehat{\theta}_{w,s}$, up to $\tau = 0.5\tau_{total}$, overlay relatively well, which verifies the scaling (11), although noticeable variations observed for different Pr values. These variations are apparently due to the effect of $[O(1) + O(\mathrm{Pr})]$, as predicted by the scalings (11) and (9) for $\theta_{w,s}$ and τ_s, respectively. However, as these variations are not significant, the effects of $[O(1) + O(\mathrm{Pr})]$ are very weak for the θ_w case, similar to the δ_T case.

3.4. Scalings for v_m

The scaling (8) at the start-up stage demonstrates that v_m depends on Ra and y. This is verified with the numerical simulation results, as presented in Fig. 7(*a*) which shows that the time series of Runs 1–4, which have varying Ra and y values, overlay each other at the start-up stage, but they vary significantly at different Pr and f_n values. The 1D behavior of the NCBL at the start-up stage is once more affirmed. At the quasi-steady state, all time series are different, agreeing with the scaling (13), which predicts that $v_{m,s}$ is dependent on Pr, f_n and y, but not of Ra, and the flow becomes 2D.

From the scaling (8), the following relation is expected,

$$\frac{v_m}{v_{m,s}} \sim \frac{\sin(2\pi f_n\tau)Pr\tau^{3/2}}{\sin(2\pi f_n\tau_s)Pr\tau_s^{3/2}} \sim \frac{\sin(2\pi f_n\tau)\tau^{3/2}}{\sin(2\pi f_n\tau_s)\tau_s^{3/2}}, \tag{35}$$

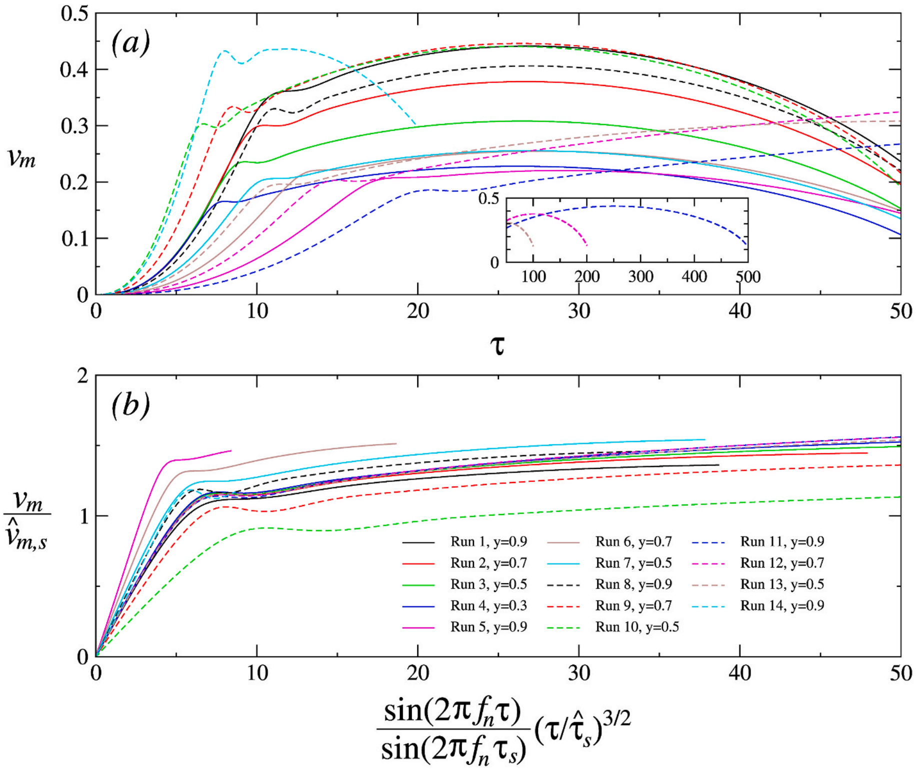

Fig. 7. Time series of v_m of all numerical simulation runs: (*a*) raw data and (*b*) scaled data with v_m scaled by $\widehat{v}_m = \mathrm{Pr}^{2/5}[\sin(2\pi f_n\tau_s)]^{2/5}y^{3/5}$ and τ scaled by $\widehat{\tau}_s = (y/[\mathrm{Pr}\sin(2\pi f_n\tau_s)])^{2/5}$, which are the scalings (13) and (9) for $v_{m,s}$ and τ_s, respectively.

which also indicates that

$$\frac{v_m}{\widehat{v}_{m,s}} \sim \frac{\sin(2\pi f_n\tau)\tau^{3/2}}{\sin(2\pi f_n\tau_s)\widehat{\tau}_s^{3/2}}. \tag{36}$$

As presented in Fig. 7(*b*), at the start-up stage, the above relation is linear for each scaled time series, *i.e.*,

$$\frac{v_m}{\widehat{v}_{m,s}} = C\frac{\sin(2\pi f_n\tau)}{\sin(2\pi f_n\tau_s)}\frac{\tau^{3/2}}{\widehat{\tau}_s^{3/2}}, \tag{37}$$

that is,

$$\begin{aligned} v_m &= C\widehat{v}_{m,s}\frac{\sin(2\pi f_n\tau)}{\sin(2\pi f_n\tau_s)}\frac{\tau^{3/2}}{\widehat{\tau}_s^{3/2}} \\ &= C\mathrm{Pr}^{2/5}[\sin(2\pi f_n\tau_s)]^{2/5}y^{3/5}\frac{\sin(2\pi f_n\tau)}{\sin(2\pi f_n\tau_s)}\frac{\tau^{3/2}}{\left(\dfrac{y^{2/5}}{\mathrm{Pr}^{\,2/5}[\sin(2\pi f_n\tau_s)]^{2/5}}\right)^{3/2}} \\ &= C\mathrm{Pr}\,\sin(2\pi f_n\tau)\tau^{3/2}, \end{aligned} \tag{38}$$

where C is a proportional coefficient, which is found to vary significantly when *Pr* changes. If Runs 5–10 with different Pr values from Pr=0.1, along with Run 14 (due to a very short quasi-steady state as discussed above), are excluded, the numerical simulation results presented in Fig. 7(*b*) give the average value of $C = 0.199$ for all the remaining runs, with very small variations in the range of -3.2% to1.8%. However, for the runs with Pr=0.01, 0.025, 0.05, 0.075, 0.2 and 0.5, the values of C vary substantially, with the variations of 73%, 44.9%, 19.8%, 12.8%, -17.8%, and -43.4%, respectively, from $C = 0.199$ for Runs 5–10, clearly showing the significant effect of Pr. Each of the scalings (8), (9) and (13) has a function of Pr term (in the form of $[O(1) + O(\mathrm{Pr})]$). But in the above equations, such a function of Pr is omitted in each scaling when the results are analysed. Thus different from that in the δ_T and θ_w cases, as shown above, the additional Pr effect is significant in the v_m case and must be accounted for in the quantified scalings. As v_m is the maximum value of v within the inner boundary layer, with its location at δ_{vi} near the wall, it is expected that Pr (representing the relative strength of convection compared to the conduction) has a much stronger effect on both v_m and δ_{vi} than on θ_T and θ_w which are parameters at the end of the outer boundary layer. The above C value represents the combined effect of Pr from each parameter on the relation.

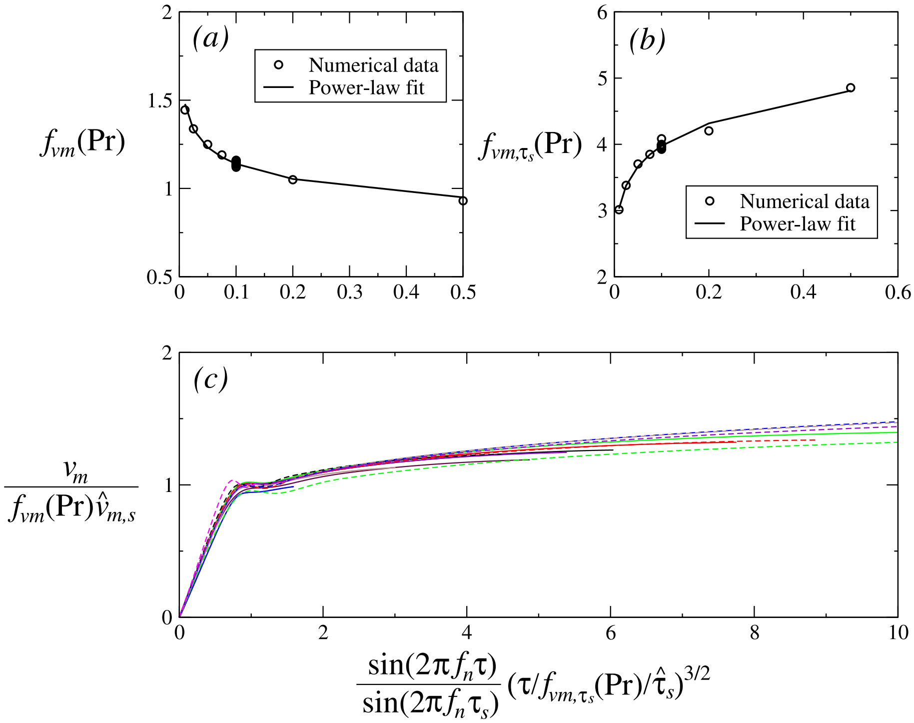

Fig. 8. (*a*) $f_{vm}(\mathrm{Pr})$ plotted against Pr, (*b*) $f_{vm,\tau_s}(\mathrm{Pr})$ plotted against Pr, and (*c*) $v_m/[f_{vm}(\mathrm{Pr})\widehat{v}_{m,s}]$ plotted against $[\sin(2\pi f_n\tau)/\sin(2\pi f_n\tau_s)](\tau/f_{vm,\tau_s}(\mathrm{Pr})/\widehat{\tau}_s)^{3/2}$. The legends are the same as that in Fig. 7.

The effects of $[O(1)+O(\mathrm{Pr})]$ on $v_{m,s}$ and τ_s can be quantified by the numerical results with the function $f_{vm}(\mathrm{Pr})$ and $f_{vm,\tau_s}(\mathrm{Pr})$, which are the values of $v_m/\hat{v}_{m,s}$ and $(\tau/\hat{\tau}_s)^{3/2}$ at the end of the start-up stage, respectively, as shown in Fig. 8(*a*) and Fig. 8(*b*). The results show that when Pr increases, $f_{vm}(\mathrm{Pr})$ decreases, but $f_{vm,\tau_s}(\mathrm{Pr})$ increases. They can be quantified by the following power-law fit curves obtained by regression from the numerical simulation results,

$$f_{vm}(\mathrm{Pr}) = 0.885Pr^{-0.112}, \tag{39}$$

and

$$f_{vm,\tau_s}(\mathrm{Pr}) = 5.221Pr^{0.118}, \tag{40}$$

with the regression coefficients of 0.9838 and 0.9934, respectively. Again Run 14 is excluded in the above fit curves due to the reason discussed above.

With the inclusion of $f_{vm}(\mathrm{Pr})$ and $f_{vm,\tau_s}(\mathrm{Pr})$ in the scalings (13) and (9), the variations in the scaled time series of v_m have been significantly reduced, as shown in Fig. 8(*c*), as they overlay each other well over the entire development duration of the boundary layer until $\tau = 0.5\tau_{total}$, although there is a noticeable deviation for Run 10 with $\mathrm{Pr} = 0.5$, which indicates that the accuracy of the correlations (39) and (40) reduces at Pr close to 1. However, when Pr becomes close to 1, the assumption of $\mathrm{Pr} \ll 1$ for the validity of the obtained scalings is no longer met satisfactorily. Nevertheless, overall it is observed that the obtained $f_{vm}(\mathrm{Pr})$ and $f_{vm,\tau_s}(\mathrm{Pr})$ correlations accurately predict the effects of $[O(1)+O(\mathrm{Pr})]$ on $v_{m,s}$ and τ_s, verifying the scalings (8), (9) and (13).

3.5. Scalings for δ_{vi}

The scaling (7) at the start-up stage shows that δ_{vi} is of Ra and Pr dependent, but not of y and f_n. This is verified by the numerical results, as presented in Fig. 9(*a*) where it is noted that all five time series at $\mathrm{Ra} = 10^8$ and $\mathrm{Pr} = 0.1$, but with changing y (*i.e.*, Runs 3, 11–14), overlay each other at the start-up stage, while there are significant variations for the runs with different Ra and Pr values. This again illustrates the 1D behavior of the boundary layer at the start-up stage. At the quasi-steady state, all time series are different, agreeing with the scaling (12), which predicts that $\delta_{vi,s}$ is dependent on Ra, Pr, f_n and y, and the flow becomes 2D.

At the start-up stage, from the scaling (7), the following relation is expected,

$$\frac{\delta_{vi}}{\delta_{vi,s}} \sim \frac{Pr^{1/2}\tau^{1/2}/Ra^{1/5}}{Pr^{1/2}\tau_{vi,s}^{1/2}/Ra^{1/5}} \sim \frac{\tau^{1/2}}{\tau_{vi,s}^{1/2}}, \tag{41}$$

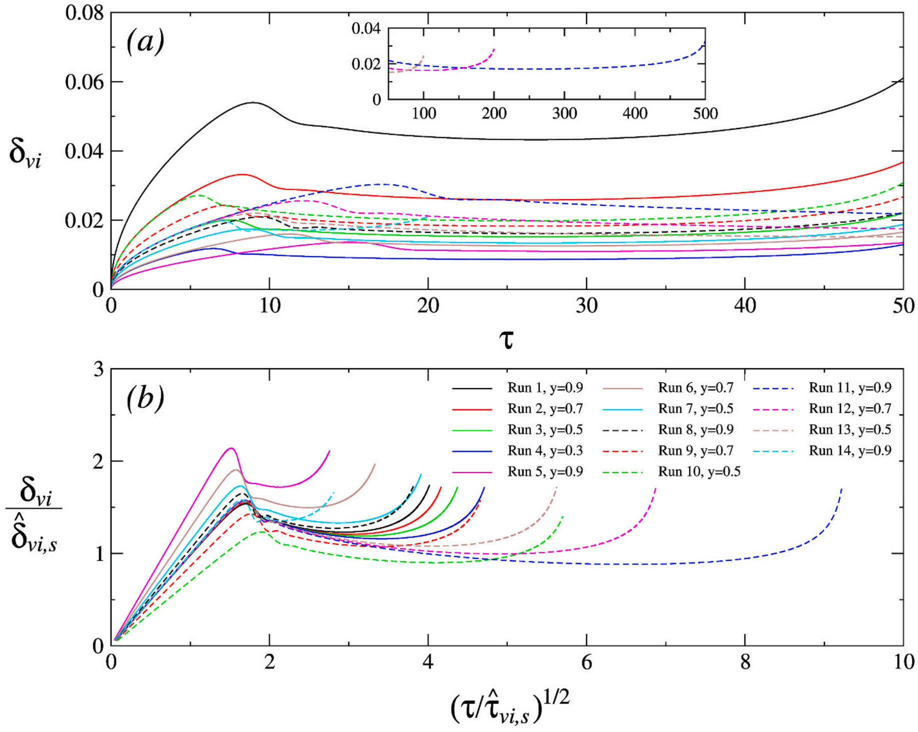

Fig. 9. Time series of δ_{vi} of all numerical simulation runs: (*a*) raw data and (*b*) scaled data with δ_{vi} scaled by $\hat{\delta}_{vi,s} = \mathrm{Pr}^{1/2}y^{1/5}/(\mathrm{Ra}^{1/5}\mathrm{Pr}^{1/5}[\sin(2\pi f_n\tau_{vi,s})]^{1/5})$ and τ scaled by $\hat{\tau}_{vi,s} = (y/[\mathrm{Pr}\sin(2\pi f_n\tau_{vi,s})])^{2/5}$, which are the scalings (12) and (9) for $\delta_{vi,s}$ and $\tau_{vi,s}$, respectively.

which also means that

$$\frac{\delta_{vi}}{\widehat{\delta}_{vi,s}} \sim \frac{\tau^{1/2}}{\widehat{\tau}^{1/2}_{vi,s}}. \tag{42}$$

This relation is validated by the numerical simulation results as illustrated in Fig. 9(*b*), as $\delta_{vi}/\widehat{\delta}_{vi,s}$ is linearly proportional to $\tau^{1/2}/\widehat{\tau}^{1/2}_{vi,s}$ for each scaled time series at the start-up stage, *i.e.*,

$$\frac{\delta_{vi}}{\widehat{\delta}_{vi,s}} = D\frac{\tau^{1/2}}{\widehat{\tau}^{1/2}_{vi,s}}, \tag{43}$$

that is,

$$\begin{aligned}
\delta_{vi} &= D\widehat{\delta}_{vi,s}\frac{\tau^{1/2}}{\widehat{\tau}^{1/2}_{vi,s}} \\
&= D\frac{\mathrm{Pr}^{1/2}y^{1/5}}{\left[\sin\left(2\pi f_n\tau_{vi,s}\right)\right]^{1/5}\mathrm{Ra}^{1/5}\mathrm{Pr}^{1/5}}\frac{\tau^{1/2}}{\left(\dfrac{y^{2/5}}{\mathrm{Pr}^{2/5}\left[\sin\left(2\pi f_n\tau_{vi,s}\right)\right]^{2/5}}\right)^{1/2}} \\
&= D\frac{\mathrm{Pr}^{1/2}\tau^{1/2}}{\mathrm{Ra}^{1/5}},
\end{aligned} \tag{44}$$

where D is a proportional coefficient and has a different value for a specific run. For the runs with $\mathrm{Pr} = 0.1$ (*i.e.*, Runs 1–4 and 11–14), $D \approx 0.986$, but it changes substantially with Pr. The values of D are 49.9%, 24.1%, 9.8%, 2%, -16.2%, and -31.9% away from 0.986 for $\mathrm{Pr} = 0.01$, 0.025, 0.05, 0.075, 0.1, 0.2, and 0.5, respectively. This is due to the effect of $[O(1) + O(\mathrm{Pr})]$ in the scalings (7), (12) and (9), similar to that for v_m. Such large variations in D among runs with different Pr values indicate that the extent of this additional Pr effect is significant, as discussed above for the v_m case.

Similar to the v_m case, the effects of $[O(1) + O(\mathrm{Pr})]$ on $\widehat{\delta}_{vi,s}$ and $\widehat{\tau}_{vi,s}$ can be evaluated by the numerical results with the function $f_{vi}(\mathrm{Pr})$ and $f_{\tau_{vi,s}}(\mathrm{Pr})$, which are the values of $\delta_{vi}/\widehat{\delta}_{vi,s}$ and $(\tau/\widehat{\tau}_{vi,s})^{1/2}$ at the end of the start-up stage, respectively, as shown in Fig. 10(*a*) and Fig. 10(*b*). It is seen that $f_{vi}(\mathrm{Pr})$ increases with Pr, but $f_{\tau_{vi,s}}(\mathrm{Pr})$ is on the contrary. They can be quantified by the following power-law fit curves obtained from the numerical simulation results,

$$f_{vi}(\mathrm{Pr}) = 1.133Pr^{-0.14}, \tag{45}$$

and

$$f_{\tau_{vi,s}}(\mathrm{Pr}) = 3.739Pr^{0.111}, \tag{46}$$

with the regression coefficients of 0.9974 and 0.9875, respectively. It is noted that in the case when the applied heat flux is constant [23], a similar power-law fit curve is obtained from numerical results for f_{vi}, with the index of -0.125, which is close to -0.14 present in the correlation (45).

With the inclusion of $f_{vi}(\mathrm{Pr})$ and $f_{\tau_{vi,s}}(\mathrm{Pr})$ in the scalings (12) and (9), the variations in the scaled time series of δ_{vi} have been significantly reduced, as shown in Fig. 10(*c*), as all of them overlay each other very well over the entire development duration of the boundary layer until $\tau = 0.5\tau_{total}$. This clearly shows that the obtained $f_{vi}(\mathrm{Pr})$ and $f_{\tau_{vi,s}}(\mathrm{Pr})$ correlations accurately predict the effects of $[O(1) + O(\mathrm{Pr})]$ on $\widehat{\delta}_{vi,s}$ and $\widehat{\tau}_{vi,s}$.

Comparing the correlations (45) and (39), it is noted that the effect of $[O(1) + O(\mathrm{Pr})]$ on $\delta_{vi,s}$ is essentially the same as that on $v_{m,s}$, with the index of -0.14 in (45) very close to the index of -0.112 in (39). This should be expected as δ_{vi} is the distance from the wall to the location of the maximum velocity (v_m) so δ_{vi} is directly governed by v_m and the effects of $[O(1) + O(\mathrm{Pr})]$ on $v_{m,s}$ and $\delta_{vi,s}$ are essentially the same.

4. Conclusions

Scalings are obtained to characterize and quantify the basic features of unsteady NCBL of a homogeneous fluid with $\mathrm{Pr} < 1$ on a vertical wall heated with a time-varying flux by following the same scaling analysis procedure used in our previous study [23] which investigated the counterpart of the present case, with the applied heat flux being constant. The scalings are developed in terms of Pr, Ra and f_n.

The dominant parameters characterizing the flow behavior are the plate temperature, maximum vertical velocity, thermal boundary-layer thickness, velocity boundary-layer thickness, and the time for the transition from the start-up stage to the steady state. The scaling analysis shows that the development of the boundary layer at the start-up stage is one-dimensional and y independent but becomes two-dimensional and is y dependent at the steady state.

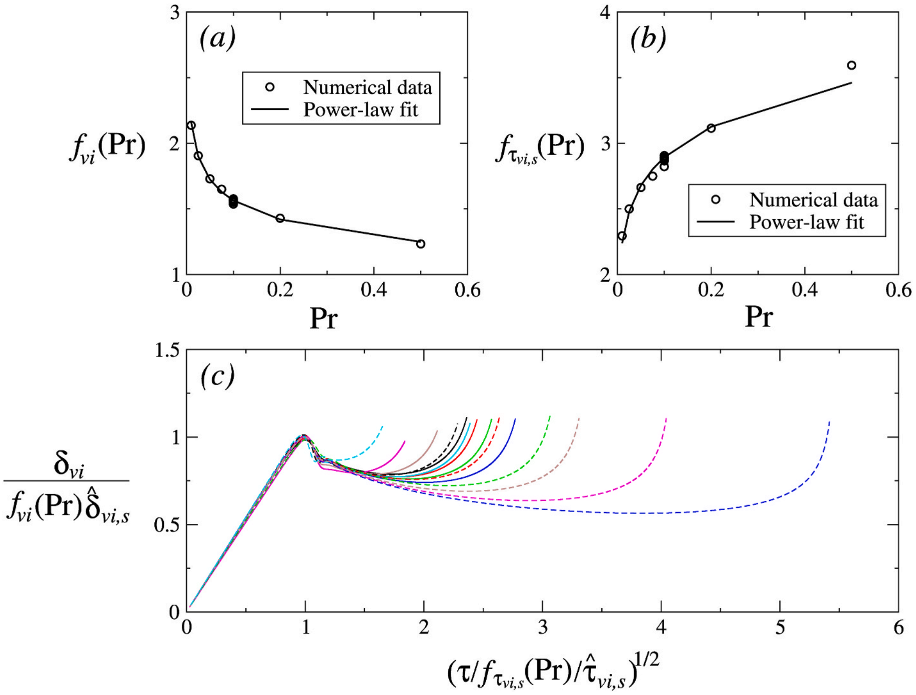

Fig. 10. (*a*) f_{vi}(Pr) plotted against Pr, (*b*) f_{vi,τ_s}(Pr) plotted against Pr, and (*c*) $\delta_{vi}/[f_{vi}(\mathrm{Pr})\widehat{\delta}_{vi,s}]$ plotted against $(\tau/f_{vi,\tau_s}(\mathrm{Pr})/\widehat{\tau}_s)^{1/2}$. The legends are the same as that in Fig. 9.

The obtained scalings are tested with 14 numerical simulation runs, over $10^6 \le \mathrm{Ra} \le 10^9$, $0.01 \le \mathrm{Pr} \le 0.5$, and $0.001 \le f_n \le 0.025$, which shows that the numerical simulation results agree well with the scalings and hence these scalings are validated. The 1D behavior at the start-up stage and the 2D behavior at the quasi-steady state of the NCBL predicted by the scalings are also affirmed by the numerical simulation results.

CRediT authorship contribution statement

Wenxian Lin: Conceptualization, Methodology, Investigation, Writing – original and revision drafts. S. W. Armfield: Conceptualization, Methodology, Editing – original draft. Mehdi Khatamifar: Review and editing - original and revision drafts.

Declaration of competing interest

The authors declare that they have no known competing financial interests or personal relationships that could have appeared to influence the work reported in this paper.

Acknowledgment

The support from the Australian Research Council (Discovery Project grant DP130100900) is gratefully acknowledged.

References

[1] J.A. Duffie, W.A. Beckman, Solar Engineering of Thermal Processes, fourth ed., John Wiley & Sons, 2013.
[2] J.C. Patterson, C. Lei, S.W. Armfield, W. Lin, Int. J. Therm. Sci. 48 (2009) 1843–1852.
[3] W. Lin, S.W. Armfield, Phys. Rev. E 88 (2013), 063013.
[4] W. Lin, S.W. Armfield, Int. J. Therm. Sci. 111 (2017) 78–99.
[5] Q.W. Wang, J. Yang, M. Zeng, G. Wang, Int. J. Heat Fluid Flow 31 (2010) 70–82.
[6] G. Wang, M. Zeng, Y.C. Ren, H. Ozoe, Q.W. Wang, Exp. Therm. Fluid Sci. 35 (2011) 105–111.
[7] S.C. Saha, M.M.K. Khan, Int. J. Heat Mass Tran. 55 (2012) 2268–2284.
[8] F. Wu, G. Wang, W. Zhou, Numer. Heat Tran. A: Applications 70 (3) (2016) 310–329.
[9] W. He, G. Qin, Y. Wang, Z. Bao, Numer. Heat Tran. A: Applications 76 (2) (2019) 51–72.
[10] Y. Liu, Phys. Rev. E 100 (2019), 043112.
[11] W. Lin, S.W. Armfield, Numer. Heat Tran. A: Applications 76 (6) (2019) 393–419.
[12] B. Nie, F. Xu, Phys. Fluids 31 (2019), 024107.
[13] T. Hattori, J.C. Patterson, C. Lei, Int. J. Heat Mass Tran. 87 (2015) 24–35.
[14] Y. Liu, Int. J. Heat Mass Tran. 154 (2020) 119767.

[15] Y. Liu, H. Huang, Int. J. Heat Mass Tran. 147 (2020) 118951.
[16] L. Zhou, S.W. Armfield, N. Williamson, M.P. Kirkpatrick, W. Lin, Int. J. Heat Mass Tran. 150 (2020) 119234.
[17] D.S. Loenko, A. Shenoy, M.A. Sheremet, Int. J. Therm. Sci. 166 (2021) 106973.
[18] W. Lin, S.W. Armfield, Numer. Heat Tran. A: Applications 77 (6) (2020) 619–631.
[19] J. Fohr, H.B. Moussa, Int. J. Heat Mass Tran. 37 (1994) 1699–1712.
[20] P. Yu, J.C. Patterson, C. Lei, Int. J. Heat Fluid Flow 38 (2012) 107–117.
[21] S.C. Saha, J.C. Patterson, C. Lei, Int. J. Therm. Sci. 49 (2010) 1899–1910.
[22] Y. Mao, C. Lei, J.C. Patterson, Int. J. Therm. Sci. 71 (2013) 61–73.
[23] W. Lin, S.W. Armfield, Phys. Rev. E 72 (2005), 066309.
[24] S.W. Armfield, J.C. Patterson, W. Lin, Int. J. Heat Mass Tran. 50 (2007) 1592–1602.
[25] W. Lin, S.W. Armfield, J.C. Patterson, C. Lei, Phys. Rev. E 79 (2009), 066313.
[26] W. Lin, S.W. Armfield, J.C. Patterson, Int. J. Heat Mass Tran. 51 (2008) 327–343.
[27] W. Lin, S.W. Armfield, Phys. Rev. E 86 (2012), 066312.
[28] W. Lin, S.W. Armfield, J.C. Patterson, J. Fluid Mech. 574 (2007) 85–108.